



This is a repository copy of *Revealing hidden information in osteoblast's mechanotransduction through analysis of time patterns of critical events*.

White Rose Research Online URL for this paper:
<http://eprints.whiterose.ac.uk/158763/>

Version: Published Version

Article:

Ascolani, G., Skerry, T.M. orcid.org/0000-0003-1319-5575, Lacroix, D. et al. (2 more authors) (2020) Revealing hidden information in osteoblast's mechanotransduction through analysis of time patterns of critical events. *BMC Bioinformatics*, 21 (1). 114. ISSN 1471-2105

<https://doi.org/10.1186/s12859-020-3394-0>

Reuse

This article is distributed under the terms of the Creative Commons Attribution (CC BY) licence. This licence allows you to distribute, remix, tweak, and build upon the work, even commercially, as long as you credit the authors for the original work. More information and the full terms of the licence here:
<https://creativecommons.org/licenses/>

Takedown

If you consider content in White Rose Research Online to be in breach of UK law, please notify us by emailing eprints@whiterose.ac.uk including the URL of the record and the reason for the withdrawal request.



eprints@whiterose.ac.uk
<https://eprints.whiterose.ac.uk/>

METHODOLOGY ARTICLE

Open Access



Revealing hidden information in osteoblast's mechanotransduction through analysis of time patterns of critical events

Gianluca Ascolani^{1,2}, Timothy M. Skerry¹, Damien Lacroix^{2,3}, Enrico Dall'Ara^{1,2} and Aban Shuaib^{1,2*} 

Abstract

Background: Mechanotransduction in bone cells plays a pivotal role in osteoblast differentiation and bone remodelling. Mechanotransduction provides the link between modulation of the extracellular matrix by mechanical load and intracellular activity. By controlling the balance between the intracellular and extracellular domains, mechanotransduction determines the optimum functionality of skeletal dynamics. Failure of this relationship was suggested to contribute to bone-related diseases such as osteoporosis.

Results: A hybrid mechanical and agent-based model (Mech-ABM), simulating mechanotransduction in a single osteoblast under external mechanical perturbations, was utilised to simulate and examine modulation of the activation dynamics of molecules within mechanotransduction on the cellular response to mechanical stimulation. The number of molecules and their fluctuations have been analysed in terms of recurrences of critical events. A numerical approach has been developed to invert subordination processes and to extract the direction processes from the molecular signals in order to derive the distribution of recurring events. These predict that there are large fluctuations enclosing information hidden in the noise which is beyond the dynamic variations of molecular baselines. Moreover, studying the system under different mechanical load regimes and altered dynamics of feedback loops, illustrate that the waiting time distributions of each molecule are a signature of the system's state.

Conclusions: The behaviours of the molecular waiting times change with the changing of mechanical load regimes and altered dynamics of feedback loops, presenting the same variation of patterns for similar interacting molecules and identifying specific alterations for key molecules in mechanotransduction. This methodology could be used to provide a new tool to identify potent molecular candidates to modulate mechanotransduction, hence accelerate drug discovery towards therapeutic targets for bone mass upregulation.

Keywords: Osteoblast mechanotransduction, Molecular network, Fluctuations, Subordination theory, Directing process, Waiting time distribution

Background

Osteoporosis is a skeletal disease, characterised by increased probability of bone fractures, that costs the NHS 1.8 billion per year, with a projected increase in cost rising to over £2.2 billion per year in 2025 [1]. The disease is a product of perturbed bone remodelling (BR) process leading to aberrant bone architecture, suboptimal extracellular matrix (ECM) properties and reduction

in bone mass [2, 3]. Consequently reduction in bone strength is observed leading to an increased fracture risk in connection with falls in domestic circumstances. BR is driven by the activity of osteocytes (OCy), osteoblasts (OB) and osteoclasts (OC) in response to mechanical and biochemical stimulation. OCs are involved in bone resorption, while OBs drive bone formation and were shown to sense mechanical stimulation [4]. Nonetheless it is widely believed that OCys are the primary mechanosensors in bone, integrating bio-mechanical signals in their microenvironment to orchestrate bone resorption and formation within the BR process. This requires transduction of extracellular signals to coordinated

* Correspondence: aban.shuaib@sheffield.ac.uk

¹Department of Oncology and Metabolism, University of Sheffield, Sheffield, UK

²Insigneo Institute of In Silico Medicine, University of Sheffield, Sheffield, UK
Full list of author information is available at the end of the article



cellular responses; ultimately modulating the ECM's material properties. Though the mechanisms governing BR has been under examination for at least 50 years, however, the intricate interplay between its components at the molecular and cellular level is not well understood [2, 3, 5–7]. Hence, improved understanding of the mechanisms to transduce mechanical stimuli (mechanotransduction) into cellular activities is fundamental to better comprehend the development of osteoporosis and the effect of related treatments [8–10].

Deformation or strain caused by mechanical loading propagates through bone structure, is detected by OBs, and primarily OCy which are embedded within the bone, via mechanoreceptors such as integrins [11–14]. After mechanosensation the mechanical signal is transformed into cellular responses via the process of mechanotransduction. Integrins are pivotal for OB activation and expression of osteogenic ECM proteins, driving osteogenic differentiation [2, 3, 15, 16]. Stretching and compression of non-homogeneous tissue locally depends on the mechanical properties of the ECM milieu, which arise due to ECM's protein composition, and consequently affects OCys and their mechanotransduction. Therefore, it is believed that mechanotransduction of the different populations of OBs and OCys drives the orchestration between BR and the process of bone adaptation over time [17].

Mechanotransduction has been investigated with experimental [8, 18, 19] and computational [20–24] approaches; but many aspects of this interaction in bone cells have not yet been explored. This is due to the experimental limitation in modelling physiological molecular events in live cells and the lack of accurate experimental techniques to validate the computational models that could predict such events [25]. Most in vitro data are obtained using stretched cells in monolayer cultures, these may have different ECM relationships to living bone, while measurements based on traction force microscopy are affected by low spatial resolution and constraints in the orientation of applied forces [26]. Conversely, in silico molecular kinetics models using molecular dynamics (MD), ordinary differential equations (ODEs) and partial differential equations (PDEs) are limited to a simulated time which is in the order of 100 ns [27, 28]. Moreover, continuous approaches lack the possibility to consider discrete and highly heterogeneous systems that can form local recurrent structures among the molecules [29–31].

To address these issues, in this study a hybrid mechanical-agent based model (Mech-ABM) was used [32] and a numerical technique for analysis of intracellular events was developed to examine combined biomechanical stimulations. The advantage of using an ABM consists in generating a complex dynamics based

on simple rules for the physical interactions that would not be easily obtainable in a continuous representation of the system and would be experimentally difficult to control [33, 34]. ABMs are suitable to mimic 3D cellular systems where the dynamics of the signalling and the occurrence of intercellular events can be tracked at the molecular scale. Furthermore, ABMs of various interacting molecules are capable of reproducing local heterogeneity with respect to the number of molecular species, although at larger spatial scale the system appears homogeneous. In our model the heterogeneity of molecular populations responding to directional and time modulated stimuli can be considered [35, 36].

The possibility of having a specific subpopulation of such molecules equal to zero, which is not a global behaviour of the system, cannot be reproduced well with molecular differential equation or with gross grained compartmentalization of the space. Indeed, the scarcity of specific populations implies that specific reactions are excluded. The interaction range gives the unit of measure that defines what is local in such models. The challenge with ABMs is that the smaller the range, the larger the computational cost to identify which molecules interact. Stochastic activation of agents given by their internal clocks add another source of indeterminism to which reactions are available for an agent at a specific time and place. This is highlighted with the utilisation of Mech-ABM to examine the link between integrin mechanical properties, mechanotransduction and cell-ECM interaction. The model forecasted that heterogeneity of integrin population is influential in modulating cellular response to mechanical excitation and the emergence of molecular mechanical memory [32]. The aim of this study was to use the Mech-ABM of the OB to study the effect of external mechanical stimuli on the local molecular events within this cell.

Specifically, the ABM simulated intracellular mechanotransduction dynamics emerging due to simultaneous modulation of mechanical excitation, the latter was simulated via the mechanical model. The modulations of mechanotransduction pathways due to these mechanical events were examined. This was achieved by analysing the presence of time structure specific to the mechanotransduction network and the analysis of fluctuations produced in the stochastic representation of the non-ergodic ABM system in terms of recurrences. This approach allowed for cutting out fluctuations sequentially at different specific time scales and analyse the results also for a system in an out-of-equilibrium condition perturbed by external mechanical signals sensed by the integrins on the membrane of the OB.

We acknowledge that some assumptions made within the model will impose a level of constraint on

how the data is interpreted, for instance that an OB is a spherical cell and that all intracellular molecules involved are homogeneously distributed within the cytoplasm and the nucleus. Another limitation is that our data is illustrating the dynamics of a single OB, while bone formation at a spatial location within bone is driven by a collection of OBs. Nonetheless, projecting the complex system of multi variable agents to the single time components does not reduce the system to a trivial process. The spatial component remains essential, and so the model predicts that within the noise of mechanotransduction

there is hidden information characteristic to each class of molecule and of the process dynamics.

Implementation

We used Mech-ABM to mimic the dynamics in the mechanotransduction pathway of a single OB during the deposition of ECM factors under external mechanical perturbations [32]. Each agent represents a specific molecule, which has a relevant role in the process of ECM formation and is included in the mechanotransduction network (see Fig. 1a). The agents move following a

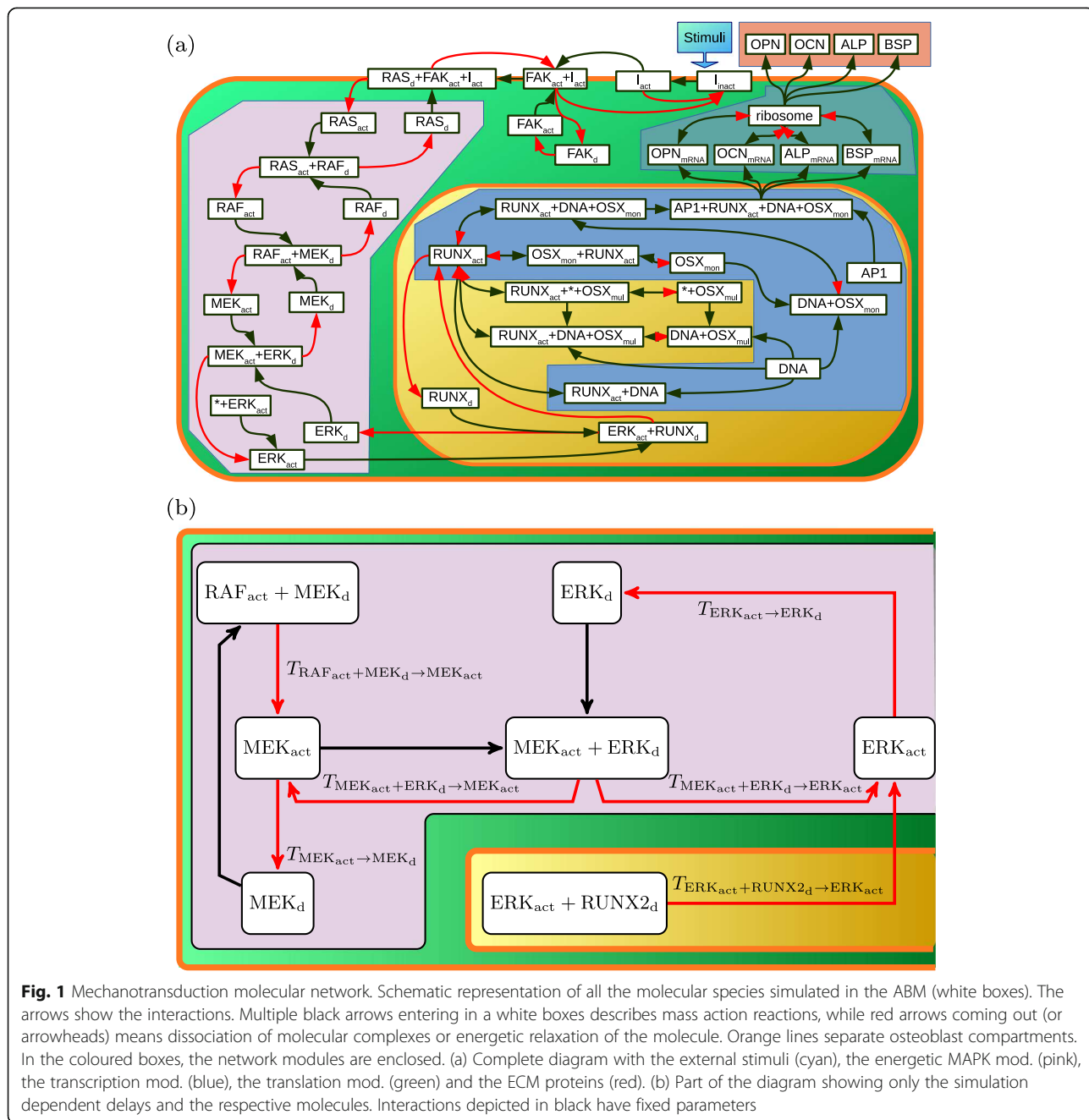


Fig. 1 Mechanotransduction molecular network. Schematic representation of all the molecular species simulated in the ABM (white boxes). The arrows show the interactions. Multiple black arrows entering in a white boxes describes mass action reactions, while red arrows coming out (or arrowheads) means dissociation of molecular complexes or energetic relaxation of the molecule. Orange lines separate osteoblast compartments. In the coloured boxes, the network modules are enclosed. (a) Complete diagram with the external stimuli (cyan), the energetic MAPK mod. (pink), the transcription mod. (blue), the translation mod. (green) and the ECM proteins (red). (b) Part of the diagram showing only the simulation dependent delays and the respective molecules. Interactions depicted in black have fixed parameters

constrained Brownian motion in one of three geometrical compartments - the cell nucleus, the cytoplasm, and the extracellular region surrounding the cell (orange borders in Fig. 1a). When the distance between two agents is shorter than the interaction range (R_{inter}), a set of rules depending on the internal state of the agents are applied to each agent involved in the interaction. Similarly, single agents can trigger rules due to their internal clock, state or information exchanged. The actions resulting from the application of rules triggered by an agent may involve:

1. The changing of its own state,
2. Self-destruction and degradation,
3. The production of information causing:
 - a. Other existing agents to change their states,
 - b. The creation of new agents, or
 - c. Triggering other actions (e.g. becoming static).

In terms of agents, the reactions between two molecules generating a molecular complex are of two types (Supplementary Fig. S1). The first requires the change of state of one agent; the second involves the change of the state of both agents. Reactions referring to a transfer of a molecular messenger are obtained by the change of the states of the agents involved. Dissociations to two or more molecules of complexes regulated by activation cycles switch (ACS) and molecular persistence in a given state have two ways. One way is the change of state of the original agents leading to appearance of a different states and the full dissociation/break-up of the complex. The other consists of state change of some agents forming the complex, thus only the molecules with changed state dissociate/break-away from the complex and consequently the complex does not fully dissociate.

Among the molecules simulated there are proteins (e.g. integrins), ribosomes, mRNA (messenger RNA) and vesicles. For the sake of simplicity, other elements like amino acids, sophisticated organelles (e.g. Golgi apparatus), molecules and complexes not included in Fig. 1a were excluded. The rules used in the proposed model are based on the affinity of the molecules, presented in said figure, that were derived from chemical reactions [24, 37, 38]. The updating scheme adopted in the model [39] requires that, at each iteration, all the molecules are aggregated and checked for possible rules to be applied. These interactions that drive the model dynamics are either: 1) binary binding of molecules based on one molecule querying all the available molecules in the sphere with radius R_{inter} and then requesting the interaction with the nearest one; 2) state transition, stabilisation and complex dissociation activated at the expiration of an internal timer set to a random time

sampled from a probability function $\Psi(t)$, when the complex changes state and decreased of 1 unit of time at each iteration.

The chemical dissociation of a complex molecule into two components occurring in the absence of other interactions with the surrounding environment due to lack of physical knowledge is described as a Poisson decay process. It follows that the times of occurrence of dissociation events are uniformly distributed. Even though $\Psi(t)$ does not give any prior knowledge of the dissociation events, it is still possible to choose the average and support of the waiting time (WTD) distribution based on experimental evidence [40, 41].

In the simulated Mech-ABM, among various signals, we generated the accumulated number of agents partitioned by their state variables mapping to their equivalent biological attributes, thus represented distinguishable molecular subpopulations (e.g. active/inactive and bound/unbound).

Stochastic processes were integrated within the Mech-ABM, whereby stochastic updates of every agent's global and local variable over time; specifically the ACS variable, were introduced [39]. Hence, simulated molecules are present in at least two complementary isoforms: active and inactive. In macroscopic steady state conditions, when one isoform produces a smooth signal close to zero axis interrupted by positive spikes, the other generates a negative fluctuation around a positive nominative value. Indeed, the process becomes immediately much more complex when there are not only active and inactive states, but also interactions with other molecular species [5, 7]. Comparing multiple simulations, it can be seen that spikes between different repetitions are not synchronized, and the time intervals between spikes of the same signal are not constant. These fluctuations, which are typical of random processes, can be difficult to associate with specific reactions in presence of a heterogeneous population of agents undergoing different interactions. Nonetheless, formation of patterns and information of the complexity of a non-ergodic system can be extracted.

Signal transformation

The agents generated by the ABM contain time-dependent information relative to their position, velocity, compartment of origin, molecular activation states, bound state and an internal clock. If each agent has n variables, and there are S agents, then the state of the system can be represented in a $n \times S$ dimensional phase space. In order to reduce the dimensionality of the systems phase space, in this study we neglected all the information relative to the position and velocity of the agents and we considered only the molecular activation state, the bound state and, when biologically relevant,

the intracellular compartment. These quantities are categorical so we can label them with discrete indices. The signals analysed are the sum of molecules with the same labelling. If each of these quantities are state variables they have values $y_i(t)$, where i is the index for the specific state variable and y is the value dependent on the time t . Given the stochastic origin of the simulations, the resulting time series are fluctuating signals, which can be decomposed in two components: the trend, $Y_i(t)$, and the fluctuations around the trend, (t) . We introduced a method to process the signal in order to obtain a positive defined time series of the noisy component by using the time average, a filter that removes the random fluctuations faster than a time lapse Δ_T :

$$\bar{y}_i(t) = \hat{A}_{\Delta_T} y_i(t) \xrightarrow{\Delta_T \rightarrow \infty} \bar{Y}_i(t),$$

where the over bar represents the time averaged signal and the operator is the moving average operator:

$$\hat{A}_T = \frac{1}{\Delta_T} \int_t^{t+\Delta_T} (\cdot) dt'.$$

This approach allowed us to cut out fluctuations sequentially at different specific time scales and analyse the results also for a system in an out-of-equilibrium condition perturbed by external mechanical signals sensed by the integrins on the membrane of the OB.

The periodic stepwise external perturbation changes the equilibrium state according to the frequency. For fast variations compared with the response of the molecules, the system remains out of equilibrium for the whole simulation while the molecules try to reach the equilibrium condition. The average of the signal, being non-constant in time, is one of the reasons why the system is not ergodic. Therefore, the trend from each signal was removed in order to obtain the fluctuations around the trend.

Subordination theory and detection of events

In this work, we propose a numerical method to disentangle random processes, called subordinated processes [42], into their respective parent process and directing process in order to analyse the latter in terms of patterns of recurrence of events [43]. A subordinate process, mathematically defined in [43–46], can be created by first generating a leading process, which can be deterministic or derived from a random distribution X , so that a trajectory x has values $x(t_i^*)$ at discrete positive times t_i^* with $t_i^* - t_{i-1}^* = \Delta t^* > 0 \forall i \in \mathbb{N}$. If we rescale the time such that $\Delta t^* = 1$ unit of time, then $t_i^* = i$ and the parent process is described by $x(t_i^*) = x(i)$

where the steps $x(t_i^*) - x(t_{i-1}^*)$ are derived from X . Then in a similar way a directing process T is generated from a random distribution with positive support such that τ_i defines a monotonically increasing function. $t(t_i^*) = \sum_{j=0}^i T_j$. The subordinated function is defined as the trajectory $x(t)$. Generally t^* is called the natural time and t is called the physical time, which is the macroscopic and experimentally observable time. The approach presented necessitated detection of critical events in the system under analysis. The system within the Mech-ABM is inherently fluctuating, leading to variation in the quantity of molecules at a given time. In order to detect the events for a molecule i , first, the time series, y_i , was filtered with a moving average over a time lapse τ_1 on each state variable, such that $y_i^I(t) = \hat{A}_{\tau_1} y_i(t)$. Then the operator \hat{A}_{τ_2} was applied, once more, to the variation of each molecular specie i from its estimated mean $\Delta y_i^I(t) = y_i^I(t) - y_i(t)$; the result of which is $y_i^{II}(t) = \hat{A}_{\tau_2} \Delta y_i^I(t)$, where the intervals of time are constrained by $\tau_1 > \tau_2$. The first moving average has been used to de-trend the time series from the signal (intended as the component with slower dynamics). The subsequent second moving average has been applied to determine the amplitude $\sigma_i(t)$ of the second moment of the non-local noise fluctuations $y_i^I(t)$ central with respect to $y_i^{II}(t)$. The term non-local is intended as non-local in time, and it includes all the times belonging to $[t - \tau_2/2, t + \tau_2/2]$ for each time t .

The time series $\Delta y_i^I(t)$ fluctuates around zero. The Hilbert transform, defined as the integral operator

$$\hat{H} = PV \int_{-\infty}^{\infty} (\cdot) \frac{d\tau}{\pi(t-\tau)},$$

has been used on the de-trended signals to derive the symmetric envelope of the de-trended signal, $y_{env}(t) = |\hat{H} y_i^I(t)|$, from which it has been subsequently detracted. The result, $y_i^{III}(t) = y_i^I(t) - y_{env}(t)$, is a positive defined time series with enhanced prominent peaks and dumped valleys close to the zero axis, Fig. 2. For each component y_i^{III} of the signal, the peaks are detected as events \mathcal{E} , if the signal minus one standard deviation of the fluctuations drops after each peak, $p_n(t)$, below the corresponding preceding peak value:

$$\mathcal{E} = \{p_n(t_1), \exists t_2 | y_i^{III}(t_2) - \sigma_i(t_2) < y_i^{III}(t_1)\}.$$

The component y_i^{III} has regions of small values; the beginning and ending of those regions are detected as events if the subtraction of one standard deviation of the fluctuations to the signal drops below or increases above the zero. The WTDs between peaks or the time extent of peaks are considered. To avoid

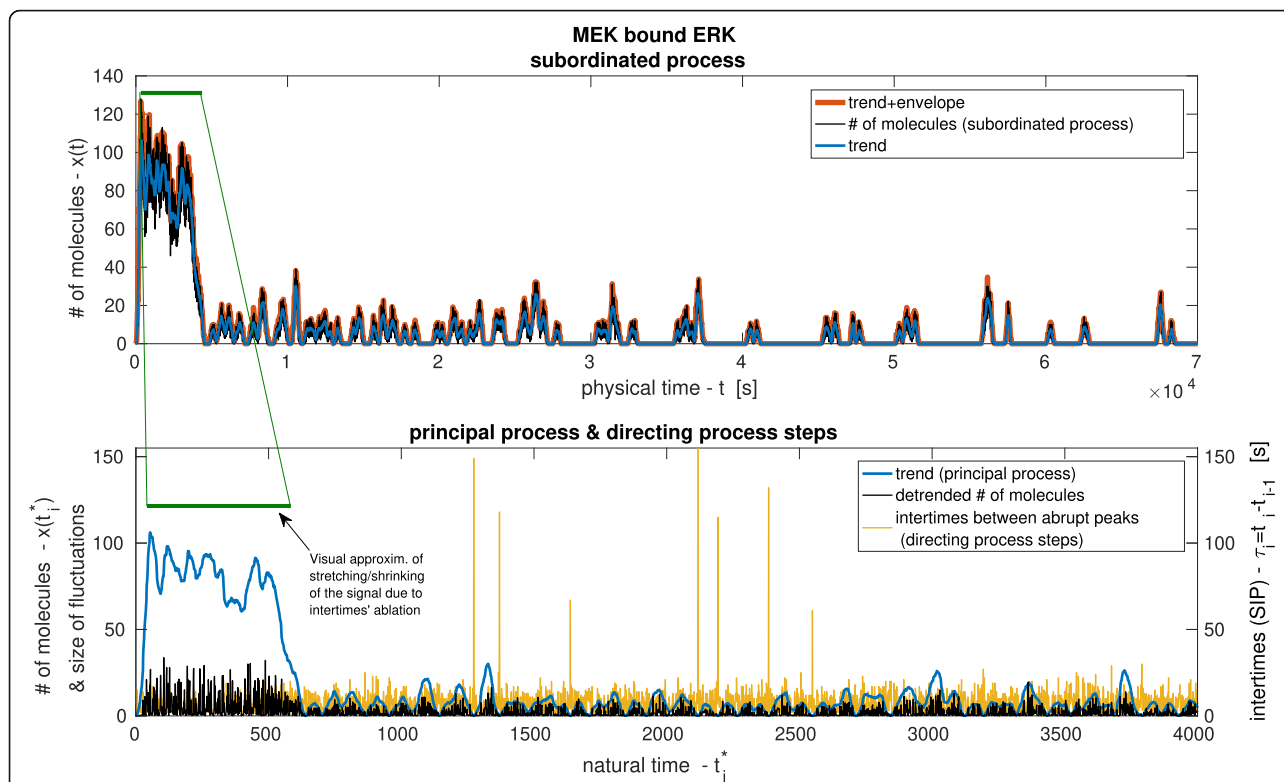


Fig. 2 Subordinated process. On the top graph, the amount of molecules for the complex MEK + ERK in function of the time t is shown. This curve represents the subordinated signal $x(t)$. The trend of the signal, derived by time average, and the envelope, derived by Hilbert transform, are used to detect the critical events. In the bottom graph, the signal interim period (SIP) τ_i between two consecutive critical events are shown in function of the physical time $t_i^* = i$. The curve $t(t_i^*)$, given by the sum of all the SIP τ up to the i^{th} event, is a realization of the directing process. In the same graph, the curve $x(t_i^*)$, given by the sum of all the steps Δx up to the i^{th} event, is a realization of the principal process. For convenience, in the bottom graph, the fluctuations around the trend are shown. In the curve $x(t_i^*)$, regions with high number of events resemble a stretched form of the subordinated signal while regions with few events manifest shrunk portions of the subordinated signal

artefacts related to fixed bin size and to be able to compare distributions obtained with different numerical parameters (in general having different binning sizes), we use a Kernel Density Estimator (KDE) defined as:

$$KDE(t) = \frac{1}{w} \int_t^{t+w} K(t-\tau)(\cdot) d\tau$$

such that $\int_{-\infty}^{\infty} K(t)dt = 1,$

w is the support of the operator.

Signal post-processing

The directing process, defined as one component of the subordinated signal and here numerically obtained by detection of critical events, provides information on the recurrences of large fluctuations of the number of molecules rapidly reaching or departing from a given node of the network, Fig. 2. The WTD of the directing process depends on the

chosen parameters so it is representative of the specific dynamics of the model. Due to the stochasticity within the model and the applied mechanical stimulation the critical events would be gamma distributed, and characterize by multimodality.

The integral distribution is first derived by weighing each signal interim period (SIP) τ between two consecutive events, $y_1^{III}(t)$ and $y_2^{III}(t + \tau)$, with the amplitude of the fluctuation $y_1^{III}(t)$. The area $\tau \times y_1^{III}(t)$ is a measure of the minimum cumulated time that molecules in a given state i , which have been involved in the same critical event, are going to spend in any state different from i . We can see it as the cumulated dispersion time of molecules sharing the same kinematics by departing from the same node of the network.

The non-normalized distribution gave the amount of the total number of molecules with the same averaged dispersion time found inside the entire duration of the sampled signal. All the signals have been de-trended and positively defined. The WTD, $\psi(\tau)$ is the probability density obtained by normalizing the integral distribution to 1.

Simulations and sensitivity analysis

In order to verify the repeatability of the results, for each set of parameters, we repeated 10 independent simulations. For each simulation, we computed the distributions, and we used the 10 independent results to derive the corresponding punctual confidence interval, (notice that the top and bottom of confidence intervals around the WTDs are not probability functions). Due to the lack of knowledge of the WTDs' dependency on any parameter, mathematically speaking, the computation of a variation of the distribution ψ is unfeasible by applying an infinitesimal affine transformation depending on a small variation of the parameters [47]. Consequently, the only possible approach consisted in running the stochastic simulations for each set of parameters analysed. This computationally expensive choice was validated by the change in modality of the WTDs shown in the results. Indeed, the model was simulated for sufficiently large variations of the parameters such that visible variations of the WTDs shape were obtained.

Given the large amount of data simulated and results generated, analyses were restricted to integrins, RUNX2, and the RAF-MEK-ERK module (Fig. 1b). These proteins and their interactions are of interest due to their role in propagating mechanical forces from plasma membrane to the nucleus of the OB; their direct involvement in mediating osteogenesis and the regulation of BR [48–50]. The results presented here are focused on the observations associated with the RAF-MEK-ERK module.

The generic ABM platform FLAME (Flexible Large-scale Agent Modelling Environment) was used to simulate intercellular mechanotransduction and mechanical loading [35, 36, 51, 52]. The simulations start with 8890 agents (Table 1) evolving with a unit time step corresponding to 1 s for a period of $9 \cdot 10^4$ s (approximately 24 h). The initial condition for the position and velocity of the agents has been chosen at random from a uniform distribution. The mechanical load used to perturb the system is mimicked by a periodic square wave function defined by its magnitude M and oscillation period P , while the phase is set to zero, and the minimal magnitude is equal to 100 μ Pa, see Table 2.

The proportions of agents belonging to specific molecular species, at time equal to 0, are constant among all the simulations performed, and their respective values are shown in Table 1. The values of the parameters for the baseline simulations are shown in Table 2.

The simulations were run at the SHEffield Advanced Research Computer cluster (SHARC) on machines with 2 x Intel Xeon E5–2630 CPUs and 64GB of RAM. Each simulation required 8GB of RAM, 96 h of execution time and approximately 500GB of hard disk space.

Table 1 Number of molecules at time $t = 0$

Molecule	#
Osteoblast cell	1
I_d	500
$I_{f \text{ act}}$	0
$I_{f \text{ act}} + \text{FAK}_{\text{act}}$	0
I_{act}	0
FAK_{act}	1000
$I_{f \text{ act}} + \text{FAK}_{\text{act}}$	1
$I_{f \text{ act}} + \text{FAK}_{\text{act}} + \text{RAS}_d$	1
FAK_d	1
RAS_d	1000
$I_{f \text{ act}} + \text{FAK}_{\text{act}} + \text{RAS}_d$	0
RAS_{act}	0
$\text{RAS}_{\text{act}} + \text{RAF}_d$	0
RAF_d	32
$\text{RAS}_{\text{act}} + \text{RAF}_d$	0
RAF_{act}	0
$\text{RAF}_{\text{act}} + \text{MEK}_d$	0
MEK_d	3400
$\text{RAF}_{\text{act}} + \text{MEK}_d$	0
MEK_{act}	0
$\text{MEK}_{\text{act}} + \text{ERK}_d$	0
ERK_d	2300
$\text{MEK}_{\text{act}} + \text{ERK}_d$	0
ERK_{act}	0
$\text{ERK}_{\text{act}} + \text{RUNX2}_d$	0
$\text{ERK}_{\text{act}} + \text{OTHER}$	0
RUNX2_d	24
$\text{ERK}_{\text{act}} + \text{RUNX2}_d$	0
$\text{RUNX2}_{\text{act}}$	0
$\text{RUNX2}_{\text{act}} + \text{DNA}$	0
OSX_{mon}	8
$\text{RUNX2}_{\text{act}} + \text{OSX}_{\text{mon}}$	0
$\text{OSX}_{\text{mon}} + \text{DNA}$	5
$\text{RUNX2}_{\text{act}} + \text{OSX}_{\text{mon}} + \text{DNA}$	0
$\text{RUNX2}_{\text{act}} + \text{OSX}_{\text{mon}} + \text{DNA} + \text{AP1}$	0
OSX_{mul}	5
$\text{RUNX2}_{\text{act}} + \text{OSX}_{\text{mul}}$	0
$\text{OSX}_{\text{mul}} + \text{DNA}$	6
$\text{RUNX2}_{\text{act}} + \text{OSX}_{\text{mul}} + \text{DNA}$	0
AP1	0
$\text{RUNX2}_{\text{act}} + \text{OSX}_{\text{mon}} + \text{DNA} + \text{AP1}$	0
OPN_{RNA}	0
$\text{Rib}_{\text{av}} + \text{OPN}_{\text{RNA}}$	0
$\text{Rib}_{\text{n av}} + \text{OPN}_{\text{RNA}}$	0
OCN_{RNA}	0
$\text{Rib}_{\text{av}} + \text{OCN}_{\text{RNA}}$	0
$\text{Rib}_{\text{n av}} + \text{OCN}_{\text{RNA}}$	0
ALP_{RNA}	0
$\text{Rib}_{\text{av}} + \text{ALP}_{\text{RNA}}$	0
$\text{Rib}_{\text{n av}} + \text{ALP}_{\text{RNA}}$	0
BSP_{RNA}	0
$\text{Rib}_{\text{av}} + \text{BSP}_{\text{RNA}}$	0
$\text{Rib}_{\text{n av}} + \text{BSP}_{\text{RNA}}$	0
$\text{Rib}_{\text{n comp}}$	299
$\text{Rib}_{\text{n comp}} + \text{RNA}$	0
Rib_c	301
$\text{Rib}_c + \text{RNA}$	0
$\text{MAT} + \text{Vesc}$	0

Table 2 Parameters' names, symbols and values

Parameter	Symbol	Value	Unit of measure
Mechanical min. magnitude	m	100	μPa
Mechanical phase	ϕ	0	rad
Integrin activation delay	$T_{I_d \rightarrow I_f \text{ act}}$	0	s
I_d dissoci. time from I + FAK comp.	$T_{I_f \text{ act} + FAK_{act} \rightarrow I_d}$	$U[0, 80]$	s
FAK _{act} activation delay	$T_{FAK_d \rightarrow FAK_{act}}$	5	s
FAK _d dissoci. time from I + FAK comp.	$T_{I_f \text{ act} + FAK_{act} \rightarrow FAK_d}$	30	s
I_{act} + FAK dissoci. time	$T_{I_f \text{ act} + FAK_{act} + RAS_d \rightarrow I_f \text{ act} + FAK_{act}}$	7	s
RAS _{act} dissoci. time from I + FAK + RAS comp.	$T_{I_f \text{ act} + FAK_{act} + RAS_d \rightarrow RAS_{act}}$	7	s
RAS _{act} dissoci. form RAS + RAF comp.	$T_{RAS_{act} + RAF_d \rightarrow RAS_{act}}$	14	s
RAS _{act} relaxation time	$T_{RAS_{act} \rightarrow RAS_d}$	60	s
RAF _{act} dissoci. time	$T_{RAS_{act} + RAF_d \rightarrow RAF_{act}}$	14	s
RAF _{act} dissoci. time from RAF + MEK	$T_{RAF_{act} + MEK_d \rightarrow RAF_{act}}$	10	s
Relaxation of RAF _{act}	$T_{RAF_{act} \rightarrow RAF_d}$	60	s
MEK _{act} dissoci. time from RAF + MEK comp.	$T_{RAF_{act} + MEK_d \rightarrow MEK_{act}}$	10	s
MEK _{act} dissoci. time from MEK + ERK comp.	$T_{MEK_{act} + ERK_d \rightarrow MEK_{act}}$	8	s
MEK relaxation time	$T_{MEK_{act} \rightarrow MEK_d}$	88	s
ERK activation time	$T_{MEK_{act} + ERK_d \rightarrow ERK_{act}}$	8	s
ERK relaxation time	$T_{ERK_{act} \rightarrow ERK_d}$	50	s
ERK _d dissoci. time from RUNX2 + ERK comp.	$T_{ERK_{act} + RUNX2_d \rightarrow ERK_{act}}$	10	s
ERK _{act} dissoci. time from ERK _{act} + OTHER comp.	$T_{ERK_{act} + OTHER \rightarrow ERK_{act}}$	6	s
RUNX2 _{act} dissoci. time from ERK _{act} + RUNX2 _d comp.	$T_{ERK_{act} + RUNX2_d \rightarrow RUNX2_{act}}$	10	s
RUNX2 _{act} dissoci. time from RUNX2 _{act} + DNA comp.	$T_{RUNX2_{act} + DNA \rightarrow RUNX2_{act}}$	10	s
RUNX2 relaxation time	$T_{RUNX2_{act} \rightarrow RUNX2_d}$	60	s
OSX _{mon} dissoci. time from RUNX2 _{act} + OSX _{mon} comp.	$T_{RUNX2_{act} + OSX_{mon} \rightarrow OSX_{mon}}$	20	s
OSX _{mon} + DNA dissoci. time from RUNX2 _{act}	$T_{RUNX2_{act} + OSX_{mon} + DNA \rightarrow OSX_{mon} + DNA}$	30	s
OSX _{mon} + DNA dissoci. time from AP1	$T_{RUNX2_{act} + OSX_{mon} + DNA + AP1 \rightarrow OSX_{mon} + DNA}$	0	s
OSX _{mul} dissoci. time from RUNX2 _{act} + OSX _{mul} comp.	$T_{RUNX2_{act} + OSX_{mul} \rightarrow OSX_{mul}}$	40	s
OSX _{mul} + DNA dissoci. time from RUNX2 _{act}	$T_{RUNX2_{act} + OSX_{mul} + DNA \rightarrow OSX_{mul} + DNA}$	50	s
ribosome availability time from Rib _{n av} + OPN _{RNA}	$T_{Rib_{n av} + OPN_{RNA} \rightarrow Rib_{av} + OPN_{RNA}}$	20	s
OPN _{RNA} dissociation time from available ribosome	$T_{Rib_{av} + OPN_{RNA} \rightarrow OPN_{RNA}}$	75	s
ribosome availability time from Rib _{n av} + OCN _{RNA}	$T_{Rib_{n av} + OCN_{RNA} \rightarrow Rib_{av} + OCN_{RNA}}$	20	s
OCN _{RNA} dissociation time from available ribosome	$T_{Rib_{av} + OCN_{RNA} \rightarrow OCN_{RNA}}$	75	s
ribosome availability time from Rib _{n av} + ALP _{RNA}	$T_{Rib_{n av} + ALP_{RNA} \rightarrow Rib_{av} + ALP_{RNA}}$	20	s
ALP _{RNA} dissociation time from available ribosome	$T_{Rib_{av} + ALP_{RNA} \rightarrow ALP_{RNA}}$	75	s
ribosome availability time from Rib _{n av} + BSP _{RNA}	$T_{Rib_{n av} + BSP_{RNA} \rightarrow Rib_{av} + BSP_{RNA}}$	20	s
BSP _{RNA} dissociation time from available ribosome	$T_{Rib_{av} + BSP_{RNA} \rightarrow BSP_{RNA}}$	75	s
RNA dissociation time from Rib _{n comp}	$T_{Rib_{n comp} + RNA \rightarrow Rib_{n comp}}$	100	s
RNA dissociation time from complete ribosome	$T_{Rib_c + RNA \rightarrow Rib_c}$	100	s
force tag probability	F_{tag}	$P_{\{01,02\}} = \{0.9, 0.1\}$	
I_d interaction radius	R_{I_d}	50	nm
FAK _{act} interaction radius	$R_{FAK_{act}}$	50	nm
RAS _d interaction radius	R_{RAS_d}	80	nm
RAF _d interaction radius	R_{RAF_d}	70	nm
MEK _d interaction radius	R_{MEK_d}	50	nm
ERK _d interaction radius	R_{ERK_d}	30	nm
RUNX2 _d interaction radius	R_{RUNX2_d}	30	nm
OSX _{mon} interaction radius	$R_{OSX_{mon}}$	30	nm
Rib _{n comp} interaction radius	$R_{Rib_{n comp}}$	30	nm
cell radius	R_{cell}	1000	nm
nucleus radius	R_{nucl}	400	nm
protein' s average velocity	\bar{v}_p	2	nm/s
protein' s velocity variation	$\overline{\Delta v_p}$	1	nm/s
protein' s direction variation	$\overline{\Delta \varphi_p} = \overline{\Delta \theta_p}$	$\pi/10$	rad
protein translation delay	T_p	95	s
transcription delay per mRNA	T_{RNA}	600	s
Integrins θ angle on cell membrane distribution	I_θ	$U[0, \pi]$	1/rad
Integrins ϕ angle on cell membrane distribution	I_ϕ	$U[0, 2\pi]$	1/rad

The effect on the fluctuations of the molecular populations were investigated by changing the magnitude M and oscillation period P of the external perturbation and the ACS of the molecular times $T_{\rightarrow \cdot}$. ($\bullet \rightarrow \bullet$ represents the initial and final transition states) for: $T_{RAF_{act} + MEK_d \rightarrow MEK_{act}}$, $T_{MEK_{act} \rightarrow MEK_d}$, $T_{MEK_{act} + ERK_d \rightarrow ERK_{act}}$, $T_{MEK_{act} +$

$ERK_d \rightarrow MEK_{act}$, $T_{ERK_{act} \rightarrow ERK_d}$, $T_{ERK_{act} + RUNX2_d \rightarrow ERK_{act}}$ (Fig. 1(b)).

All combinations for $N_M = 2$ values of the perturbations magnitude, $N_p = 3$ values of the perturbations period, and $N_T = 5$ values for each of the 6 dissociation/ACS times has been analysed, and the

Table 3 Parameters ranges: Names, symbols, unit of measures and list of values simulated. Bold quantities represent the baseline values. Where no baseline is present, then all possible combinations has been considered. Each set of parameters has been independently repeated 10 times

Parameter	Symbol	List of values	Unit of measure
Mechanical max. magnitude	M	{1000, 10000}	μPa
Mechanical period	P	{10000, 50000, 2000000}	s
MEK _{act} dissociation time from RAF _{act} + MEK _d comp.	$T_{RAF_{act}+MEK_d \rightarrow MEK_{act}}$	{ 10 , 90, 300, 480, 1320}	s
MEK _{act} dissociation time from MEK _{act} + ERK _d comp.	$T_{MEK_{act}+ERK_d \rightarrow MEK_{act}}$	{ 8 , 90, 300, 480, 1320}	s
MEK _d relaxation time	$T_{MEK_{act} \rightarrow MEK_d}$	{ 60 , 90, 300, 480, 1320}	s
ERK _{act} activation time	$T_{MEK_{act}+ERK_d \rightarrow ERK_{act}}$	{ 8 , 90, 300, 480, 1320}	s
ERK _d relaxation time	$T_{ERK_{act} \rightarrow ERK_d}$	{ 90 , 300, 480, 600, 1320}	s
ERK _{act} dissociation time from ERK _{act} + RUNX2 _d comp.	$T_{ERK_{act}+RUNX2_d \rightarrow ERK_{act}}$	{ 10 , 90, 300, 480, 1320}	s

explored parameter values were reported in Table 3. Each simulation has been repeated 10 times for a total of 1800 simulations. Analyses and additional results derived by the simulations are stored in Google Drive (https://drive.google.com/drive/folders/1Q0HFuvmv6NTxpBXfKQerR93I-4_t9LAu?usp=sharing).

Phenomenological model and constraints

In Mech-ABM the number of simulated intercellular molecules is much smaller than in the real biological system, due to the large resources, in terms of memory and computational costs, required for simulating ABMs in magnitude $\geq 10^9$ of agents. This represents an upper limit in the number of agents which can be simulated. Another limit is given by spurious behaviours introduced by finite size and finite volume effects [53] representing an inferior boundary condition for the number of agents in the model. In our case, we have an average increasing number of agents during the simulation, which limited us in the initial maximum number of molecules. Nevertheless, the model does not explicitly include any finite volume exclusion among molecules. Furthermore, the proportions of some molecules such as integrins in a specific state on the cell membrane are strongly driven by the external perturbation independently from the total number of integrins simulated. This phenomenological aspect overrides many finite size effects. Consequently, we assert that we can rescale the concentrations of the molecules and maintain the same averaged dynamic of the system by rescaling the interaction range R_{inter} of the molecules accordingly [36, 53].

Results

Waiting time distributions and spectrograms

Dissociation times/ activation cycle

As MEK and RAF interact, Raf-MEK complex forms, MEK is activated by phosphorylation, the Raf-MEK

complex dissociates, and consequently activated MEK propagates mechanotransduction. Therefore, activation dynamics of the Raf-MEK complex governed by positive and negative feedback loops dictate the complex dissociation. Hence activation-deactivation cycles are used interchangeably here. This was also observed for other complexes such as MEK-ERK. Figure 3 shows that the fluctuations of the complex RAF-MEK presents two distinct dynamics depending on the dissociation time. For dissociation time $T_{RAF_{act} + MEK_d \rightarrow MEK_{act}}$ of approximately 10 s, and varied mechanical oscillatory periods, the WTD is a bimodal distribution with modes around the recurrence times $\tau_1 = 4$ s and $\tau_2 = 9$ s, Fig. 3c. The distribution $\psi(\tau_1)$ is approximately 15% larger than in τ_2 . When $T_{RAF_{act} + MEK_d \rightarrow MEK_{act}}$ is increased from 90 s to 1320 s, the fluctuations dynamics changed; the peak at τ_1 was reduced significantly and the distribution has only one relevant maximum at $\tau = 9$ s. At $T_{RAF_{act} + MEK_d \rightarrow MEK_{act}} = 1320$ s the integrated distributions and the WTD show that a large portion of the Signal Interim Period (SIP) fluctuations are close to the mode and the occurrence of critical events is more regular. For $T_{RAF_{act} + MEK_d \rightarrow MEK_{act}} = 10$ s, we also see the number of molecules with the same dispersion time is below 200 for any delays and any period (P) of the mechanical stimulation, while it is larger than 400 at τ_2 for dissociation times $T_{RAF_{act} + MEK_d \rightarrow MEK_{act}} > 10$ s.

Reducing the values of ACS causes an increase of molecular interactions and a corresponding effect on the number of fluctuations in the signals. Such a phenomenon can be seen in non-normalized histograms of bounded molecular complexes like RAF + MEK, Fig. 4a and Fig. 5a. Instead, free molecules show a direct relation between the size of the fluctuations and the dissociation/deactivation value, Fig. 4b-c and Fig. 5b-c. Nevertheless, we have observed that the tendency of higher amount of events for smaller value of ACS ($T_{\rightarrow,} < 1320$ s) does not always hold; see Fig. 6 a-c. In such cases, after the initial increase of the number of events, there is saturation. Decreasing ASC ($T_{\rightarrow,} < 1320$ s) further cause a variation in the dynamics, and the quantity of critical events becomes

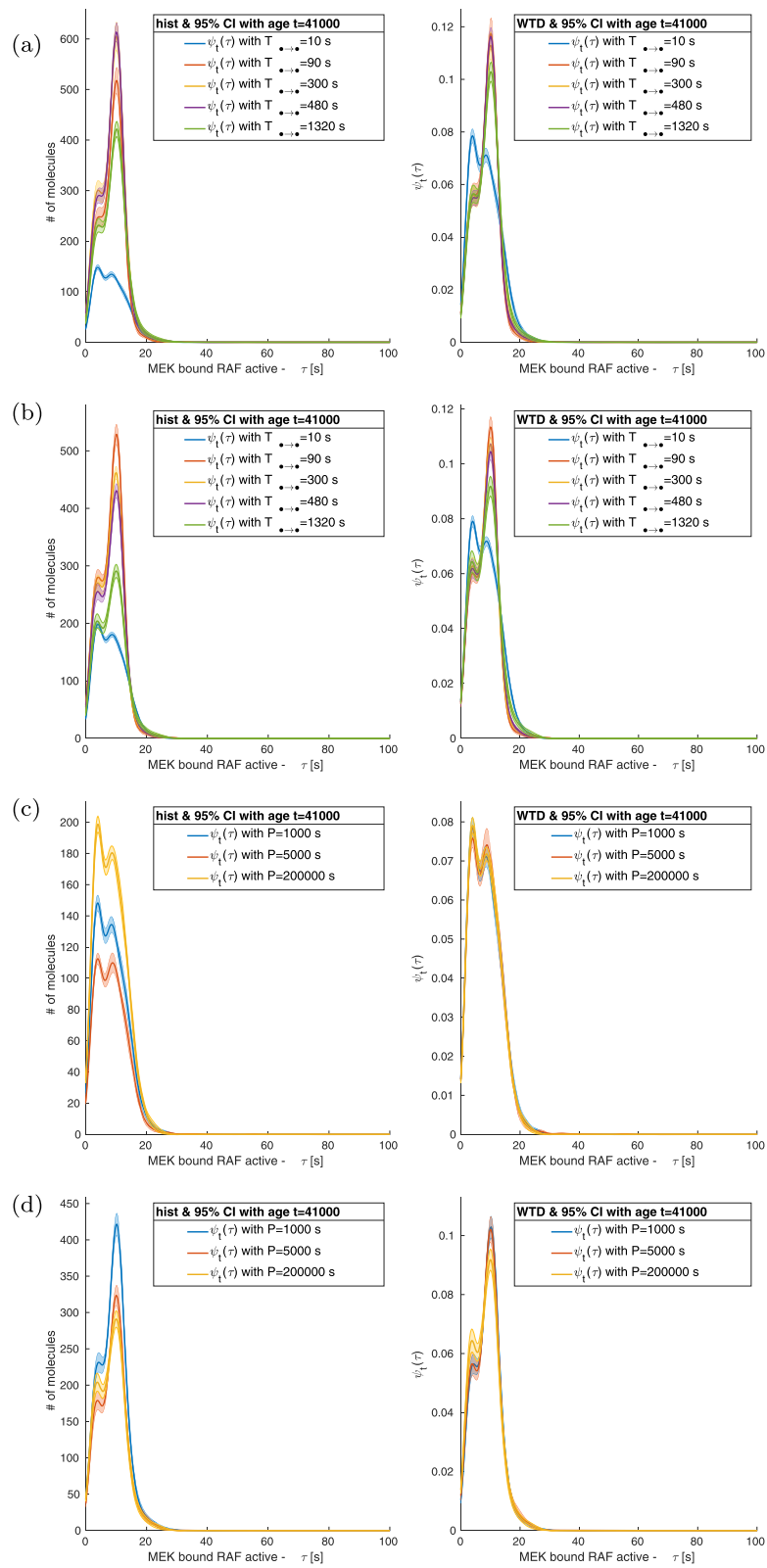


Fig. 3 (See legend on next page.)

(See figure on previous page.)

Fig. 3 MEK bound RAF. Independently from the frequencies of the tested perturbations, the variation of $T_{\text{RAFact} + \text{MEKd} \rightarrow \text{MEKact}}$ leaves the MAPK sub module of the network unchanged except for the MEK interacting with RAF which is highly sensitive to the parameter. Indeed, the distribution of recurrence of events for active MEK bounded to RAF is bimodal in $\tau = \{4, 9\}$ s. For small value of $T_{\text{RAFact} + \text{MEKd} \rightarrow \text{MEKact}} \sim 10$ s the distribution is mainly centred around $\tau = 4$ s and it represents the main mode, while for larger value of $T_{\text{RAFact} + \text{MEKd} \rightarrow \text{MEKact}}$ the distribution's main mode is at $\tau = 9$ s. **(a)** $T = 1000$ s; **(b)** $T = 200,000$ s; **(c)** $T_{\text{RAFact} + \text{MEKd} \rightarrow \text{MEKact}} = 10$ s; and **(d)** $T_{\text{RAFact} + \text{MEKd} \rightarrow \text{MEKact}} = 1320$ s

directly proportional to the value of the relaxation/dissociation time.

Mechanical perturbations

The functional form of the external perturbation is a periodic square wave which is completely characterized by the amplitude M and the period P , while the phase is set to zero, and the minimal magnitude is equal to 100 arbitrary unit (au), see Table 2. In the range of values of P investigated, two were much shorter than the total duration of each epoch, and in one case the period was set so that the stimulation applied was constant for the entire simulation. The external force activated mechanotransduction cascade and the dynamic of the system which, otherwise, would remain trapped in its initial condition. For all the analysed epochs and the simulated periods, the results indicated that the perturbation function as a switch. When the perturbation goes to its minimum, integrin activation approaches zero, and eventually other molecules in the pathway follow this trend. For all the molecules which are downstream in comparison to the integrins, the larger their network distance is, the larger their delays are in following the dynamics of the external perturbation (Fig. 1a).

The passage of the mechanical loads from high to low and vice versa is of the order of 1 time unit (1 s), and the duration P of each regime is at least 1000 s long (see Table 2 and Table 3). Indeed, all the WTDs analysed have a support shorter than all P considered, and in Figs. 3, 4, 5 and 6, the recurrence of events does not require a time larger than 100 s.

The paucity and sparsity of the events characterized by the high/low transitions of the external perturbation do have a minor effect on the SIP τ between molecular events, even in cases where the dynamics of large quantities of molecules synchronize with the external signal. On the contrary, during the time period P , molecules have the chance to form compounds or dissociate multiple times, and these events, induced by the faster molecular dynamics, account for most of the statistics shown in the WTDs.

The increase of the magnitude M of the perturbation resulted in an increase of the number of molecules activated which can be clearly observed from the variations in the non-normalized histograms, but this does not always correspond to a significant change in the distributions of the SIP.

Increasing the period P implies larger lapse of time in which the mechanotransduction is switched on. Consequently, a larger number of events are expected. If the dynamics of the system does not change during the oscillations of the perturbation, then the area under the histograms increases with the increase of P , while the WTDs do not change.

Ageing

The integral distribution and the WTD are quantities computed over a time period and are named the epoch, and are much larger than the support of the represented distributions but smaller than the total length of the simulation. Because the system is in a non-equilibrium condition, we cannot state that the WTD does not depend on the epoch so the WTD can be rewritten as $\psi_t(\tau)$ where t is the initial time of the epoch of fixed extension used for the computation. Larger epochs reduce the lack of statistics and noise, while smaller epochs allow us to compute $\psi_t(\tau)$ by choosing the age t from a larger range of available values. We tested different epoch sizes, and we compromised for a period of 10,000 s.

Ageing is characteristic of all the interacting agents, even though it is not so easy to estimate the effects of the passage of time in the histograms and WTDs, due to large confidence intervals and noise therein. Indeed, for some parameters and molecules, both the histograms and WTDs show alternate upsurge and decline patterns, and irregular cyclical variations. Even if the system is maintained in an out of equilibrium condition, the dynamics of the system responds and adapts accordingly to a mechanical perturbation.

Ageing is a direct consequence of the initial conditions; nevertheless, given that the system is regularly far from the equilibrium, ageing is prevalently due to a variation of regimes in the dynamics of the system. Therefore, the state of the system at $t=0$ should not be seen as a static initial condition, but as if the system reached such a state due to a specific long standing dynamics. Indeed, we have simulated a case where the cell had been stimulated with two consecutive trains of oscillating perturbations with different frequencies. The resulting histograms show there was no ageing at the end of the first perturbation and that ageing appeared during the second regime.

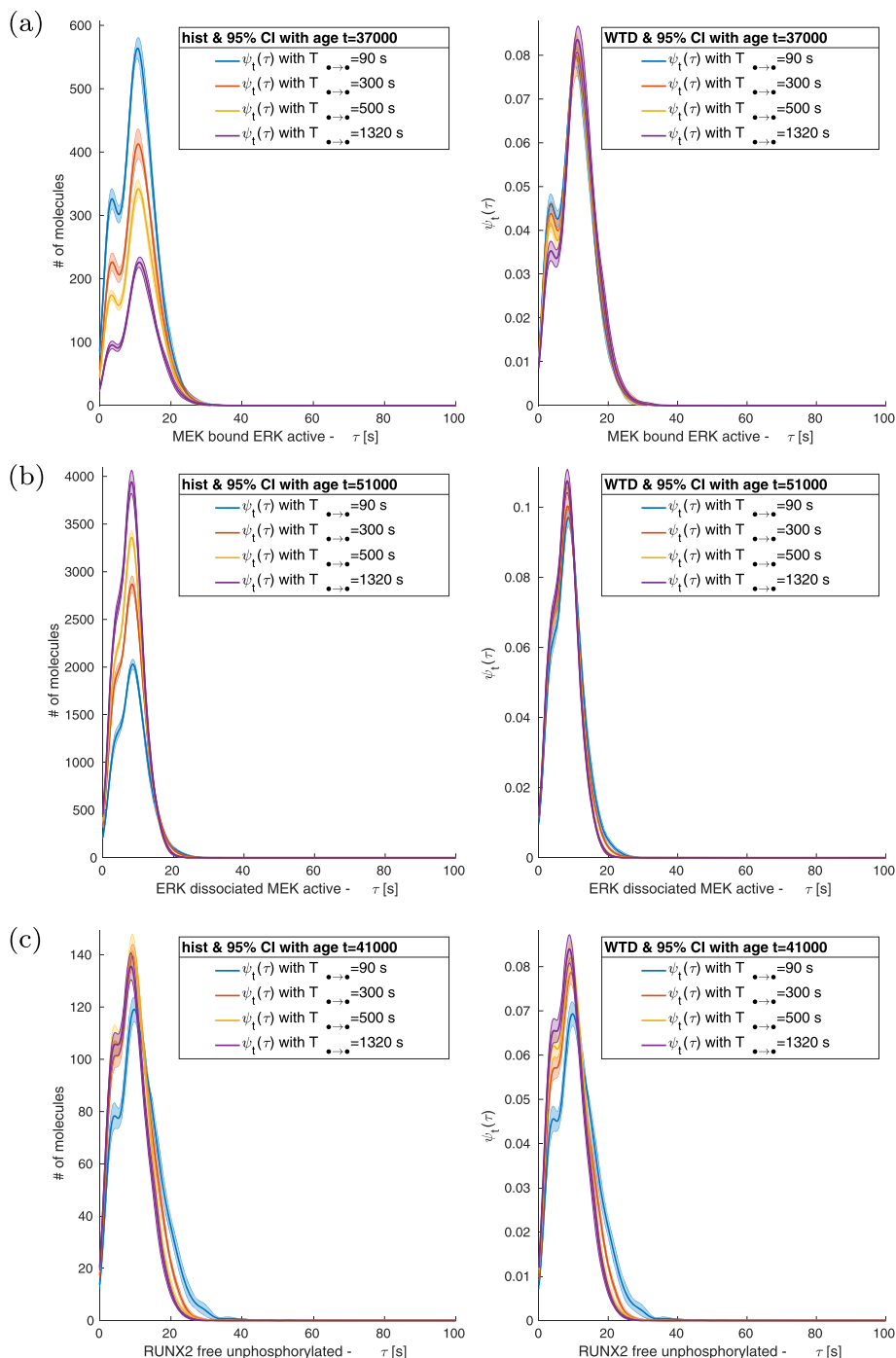


Fig. 4 MEK + ERK, ERK and RUNX2. Distributions for different values $T_{ERK_{act} \rightarrow ERK_d}$ under a periodic perturbation with $P = 1000$ s and $M = 10,000$ μPa . $T_{ERK_{act} \rightarrow ERK_d}$ produces larger effects on the next nearest neighbour of the network like unphosphorylated RUNX2 and unphosphorylated ERK. Variations in the distributions and in the non-normalized histogram of MEK bounded to ERK. No effects are visible on the distribution of active ERK dissociated from MEK. Amplitudes or number of fluctuations of ERK dissociated MEK increase with the increase of $T_{ERK_{act} \rightarrow ERK_d}$, while they show an inverse relation for MEK bound to ERK decrease

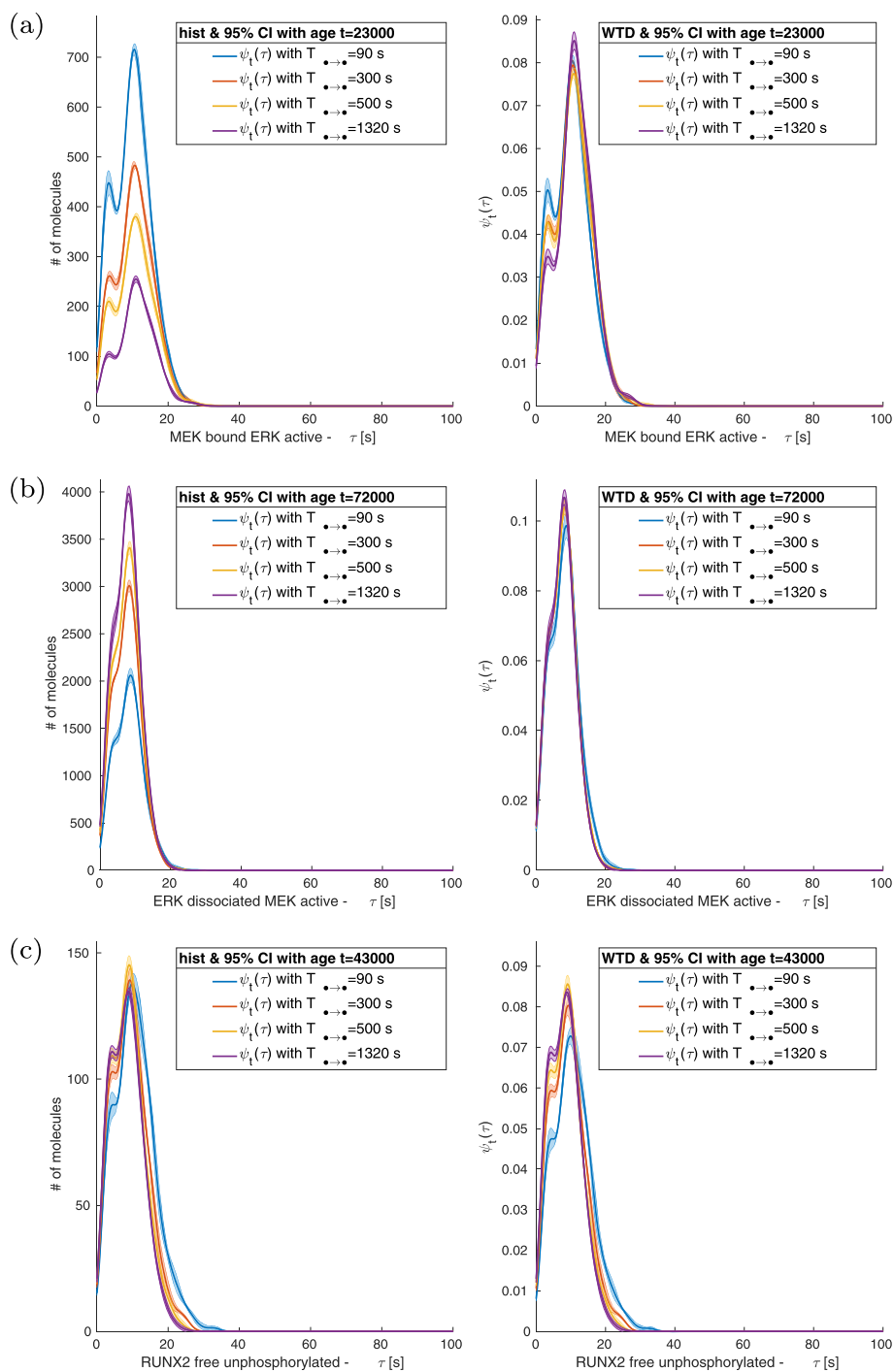


Fig. 5 MEK-ERK, ERK and RUNX2. Distributions for different values of $T_{ERK_{act} \rightarrow ERK_d}$ under a periodic perturbation with $P = 200,000$ s and $M = 10,000$ P a. The distributions are similar to those obtained with higher frequency stimulation. The histograms show larger or more frequent fluctuations of unphosphorylated RUNX2 and MEK bound ERK

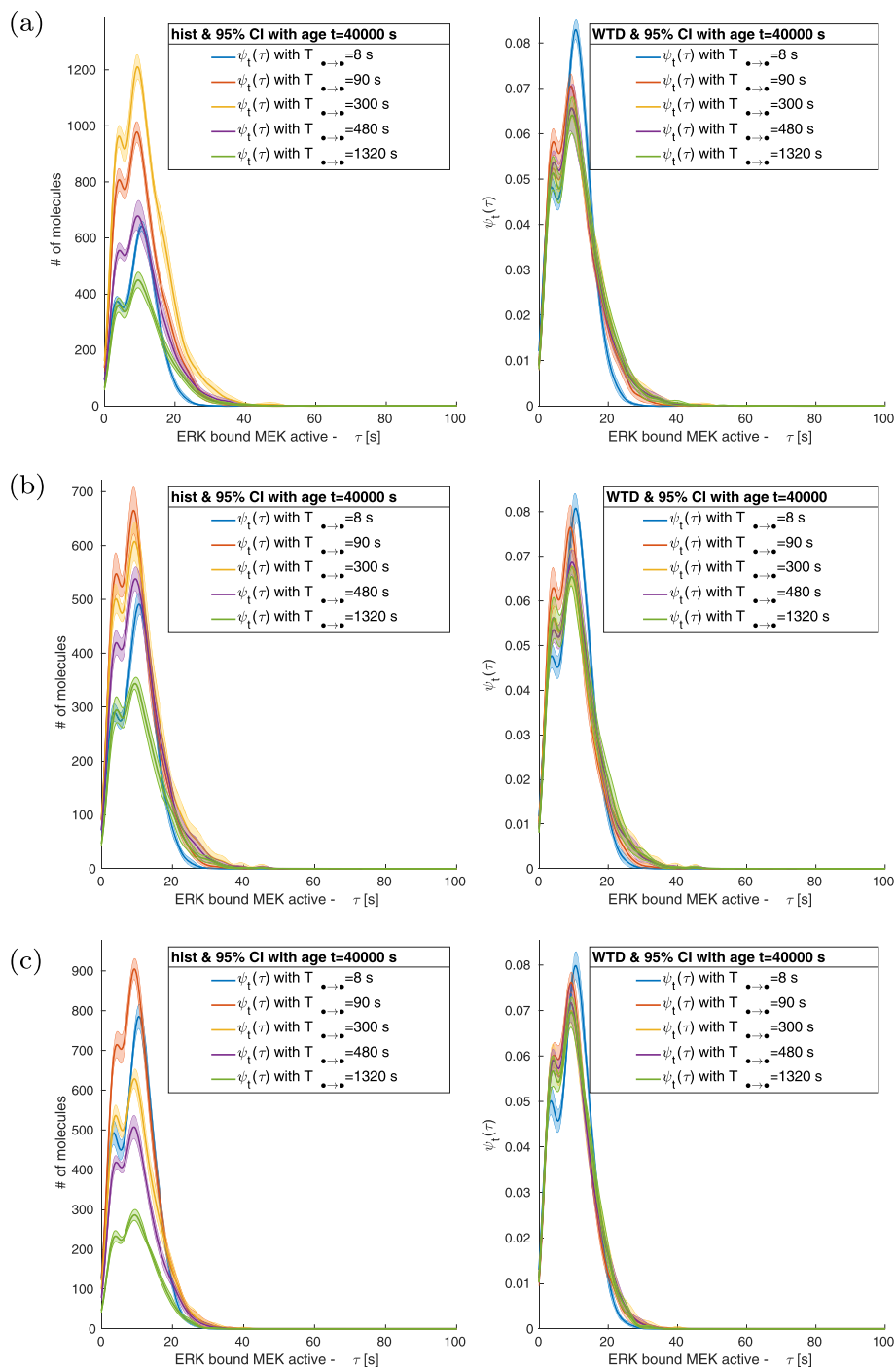


Fig. 6 ERK-MEK complex. The distributions of SIP for the ERK + MEK complex WTDs are bimodal. The modes are at T equal to 4 s and 15 s. When $T_{MEKact + ERKd \rightarrow ERKact} = 8$ s, the mode at T = 15 s shifts to 17 s. The non-normalized histograms on the left column show that the total number of events is at the minimum when $T_{MEKact + ERKd \rightarrow ERKact}$ has the maximum value simulated equal to 1320s. The number of critical events increases when $T_{MEKact + ERKd \rightarrow ERKact}$ decreases and reaches a critical value after which the dissociation time is directly proportional to the number of events

Discussion

The study illustrated that within the noise of mechanotransduction lies important information relating to the dynamics of the process. This was observed with alteration of mechanical stimuli, and modification of ERK pathway feedback loops. The study also identified innovative molecular targets, thus new therapeutic approaches to develop for osteoporosis. These involve the mimicry of mechanical stimulation, at the mechanotransduction level, by interfering with the interactions and activation states of the Raf-MEK-ERK signalling module. This was feasible using an analysis via WTD method which detected eloquent information from the noise of mechanotransduction.

Implication of simultaneous modulation of mechanical load and mechanotransduction

The dynamics of various molecules involved in an OB's mechanotransduction has been addressed in the Mech-ABM. Whereby the mechanical stimulation was modulated in terms of magnitude and period of activation (P), i.e. load frequency; while with respect to mechanotransduction, adjustments were by altering activation-deactivation cycles (i.e. feedback loops). Preliminary analyses on the resulting signals showed the external mechanical perturbation functions as a switch, but did not suggest any further synchronization on time scales smaller than the time period of the external mechanical loads. The magnitudes of activated molecules increased with respect to the value of mechanical load applied at the tissue level, specifically proteins such as phosphorylated ERK (pERK), in line with physiological observations [54, 55]. The magnitudes of molecules in time were driven by a slower dynamics frequently interrupted by asynchronous large fluctuations. The reported observations particularly with respect to the magnitude and oscillatory trend of pERK, are similar to what Grabowski et al. demonstrated with respect to pERK pulsating activity [56]. Their work showed that pERK activation pattern is linked to the stimuli's mode, though in their study the stimuli was epidermal growth factor (EGF) not mechanical. Nonetheless, Grabowski examination of the influence of different feedback loops illustrated that SIP is a mechanism by which cells can transmit information at high bit rates. This mechanism is equivalent to neuronal information processing. Considering that previously OB and OCy interpretation of mechanical signal was linked to neuronal response to excitatory events [57–59], the significant role SIP play in OB's mechanotransduction becomes clear, i.e. the utilisation of SIP to code for, and store previous mechanical information. It is worthy of note that though mechanical load altered the magnitude and modality of activated molecules, it did not significantly alter the

modalities in terms of WTDs. Changes in the WTDs were significant due to the small local error estimated from the distributions. Conversely, the frequency of applied load had more significant impact on shifting mechanotransduction dynamics, in terms of WTDs and their modalities (seen more evidently in Fig. 5). This emergent behaviour is also observed under physiological conditions where load frequency has more impact on bone formation [60–62].

The WTD of Raf, MEK and ERK molecules presented multimodality which highlights the presence of preferred SIP in the occurrence of events. Changes in the activation and deactivation cycles between molecules in the RAF-MRK-ERK module showed variations in WTDs of molecules belonging both to the classes near one of the perturbed edges and to other modules of the mechanotransduction network. For example, when $P = 1000$ s, the WTD of RAF bound to MEK was characterized by a bimodal distribution for low values of active MEK dissociation times, while it became unimodal at larger value of the same parameter. This is of significance due to the role of ERK module in mechanotransduction and the emergence of molecular memory [63, 64]. Furthermore, this is in line with Mitra et al. predictions that the oscillatory behaviour and SIP within the MAPK pathway form a mechanism where the cell stores previous stimuli as “short memory” [65]. Their observations were attributed to the flux imbalance of proteins Raf-MEK-ERK in their phosphorylation cycles, which is what Mech-ABM simulated by modulation of mechanotransduction activation cycles. Moreover, the concept of mechanical molecular memory has been described and demonstrated by Yang et al., however, their initial work only demonstrated that at the level of the transcription factor YAP/TAZ. Nonetheless the cascade linking mechanoreceptors, such as integrins, and YAP/TAZ has not yet been fully characterised, though ERK activation was previously linked with modulation of ECM stiffness. Our previous work with Mech-ABM further emphasises the link between mechanoreceptors and emergence of molecular mechanical memory, through the activation dynamics of pERK [32]. This is promising considering that recently Yang JM et al. demonstrated that ERK and its cascade are pivotal in linking mechanical and chemical signal via ERK oscillatory activation dynamics [55]. Our study forecasts that Raf-MEK-ERK module is important for mechanical-information transfer, decoding it as SIP, and providing a signature for mode of mechanotransduction.

Furthermore, via the Mech-ABM and the analysis method, shifts in WTDs' modalities were observed at the level of gene expression events. These were reflected by many of the mRNAs WTDs which were affected by ageing, a variation of the shape from a bimodal to trimodal distribution, showing the emergence of a new preferred

SIP of events manifestation. Variation in the modes implies variations in the dispersion times between chained events of the molecular network.

Currently molecules such as PTH analogue (iPTH) are used as a treatment for osteoporosis to trigger an increase in bone mass. The current view, based on the principle of mechano-regulation proposes that combining mechanical and biochemical treatment (via iPTH) can achieve optimal bone formation. The PTH receptor (PTHR) in OBs was demonstrated to recruit MEK-ERK during its endocytosis, impacting OB activation overtime via PTHR recruitment of β -arrestin scaffold proteins [66, 67]. In the presented study, the Raf-MEK-ERK module was shown to act as gatekeepers for mechanotransduction when mechanical load is applied, which is a growing view in bone mechanobiology [57, 63, 64, 68–72]. The study also forecasted that modifying the module activation can significantly shift mechanotransduction and overall state of the system. Hence we propose that the design of small molecules interfering with the Raf-MEK-ERK module activation, by perturbing their binding-interaction will allow for a shift in mechanotransduction, which can significantly amplify OB response to mechanical stimulation. These could be achieved by interfering with their interaction with scaffold proteins, such as β -arrestins, to target PTHR signalling; or Paxillin and GIT1 to affect focal adhesions signalling. Consequently, osteoporotic patients will require very mild mechanical activation, if any, via localised vibrating devices to induce a therapeutic effect in combination with anabolic treatment such as iPTH. This is plausible considering the advances in developing small-molecule drugs interfering with intracellular scaffold proteins, and their success in clinical trials [73–75].

Analysis of mechanotransduction noise

In this presented work, the abrupt fluctuations departing from the trend have been explored, analysed and presented as modalities in terms of magnitude of active molecule and WTDs. This has allowed for extraction of hidden information characteristic to each class of molecule, and overall mechanotransduction dynamics. Activation of intracellular mediators is reliant on availability of molecules and their activation states [22]. The underlying mechanisms resemble a chained Feynmans blending single molecules into signals and fluctuations at the meso/macroscopical scales. Thus finding the absolute maxima within multiple activation phases or mechanical triggers is not trivial. Consequently, a time average operator was applied as a filter to define significant mechanotransduction events, which was more appropriate in comparison to a standard ensemble average [76]. Therefore, there are no real means for the molecules with a finite interaction range to perceive a global average signal.

Hence, for a biological complex system, a time average operator is more meaningful for comparing fluctuations against the trend of the system. As the system demonstrated an average molecular signal that is intermittent in time it exhibited non-ergodicity. Thus, this necessitated transformation of the filtered signal, where the trend around the signal was removed to acquire fluctuations around the trend. In many physical and biological systems the variation of a signal is delayed by the presence of internal structures and processes that are not easily accessible to experimental observations [47]. Therefore, in these cases, the approach in the study dealt with signals showing extra layers of complexity. Therefore, the disentangling of the subordinated process is not unique, and so the preferred approach was to address the problem numerically by the identification of critical events in the system under analysis. It is reasonable to define critical events as the large and abrupt fluctuations in each molecular species due to the stochasticity of the events that the Mech-ABM captures. This is in contrast to more traditional approaches, where noise has been adopted as a measure to quantify the error around the expected values of time dependent signals [76, 77].

Limitations

The model had generated plausible predictions regarding the shift in the dynamic of cell response to mechanical stimulation when the mechanical stimulus and intracellular feedback loops were altered. We acknowledge that some assumptions made within the model will impose a level of constraint on how the data is interpreted, for instance that an OB is a spherical cell and that all intracellular molecules involved are homogeneously distributed within the cytoplasm and the nucleus. Another noteworthy limitation is that our data is illustrating the dynamics of a single OB, while bone formation at a spatial location within bone is driven by a collection of OBs. Additionally, what control BR process is the cell-cell interaction between OBs, OCys and OC, which is outside the scope of the Mech-ABM. It will be interesting to see if upscaling the presented findings to a population of many OBs interacting with OCys and OCs will induce a nudge effect that will ultimately enhance bone formation in different sites in bone tissue.

We also acknowledge that the model did not include all cell signalling mechanisms which drive bone formation, particularly WNT signalling. However, given that WNT and ERK pathway crosstalk, therefore our integration of a black-box approach to simulate ERK feedback loops, introduces WNT influence on ERK to some degree. Nonetheless, the effect of ERK signalling on WNT could not be integrated as it is not part of the mechanotransduction pathway. Yet, the Mech-ABM can be extended to include these elements easily for future

investigations to study the impact of WNT on mechanotransduction and ultimately bone formation.

Conclusions

This study simulated modulation of mechanical load and alterations in mechanotransduction feedback loops, on cellular response to mechanical stimulation. The study demonstrated that WTD of some molecule, particularly within the ERK cascade, is a dynamic marker which can be used as a signature for the system's dynamics in normal and pathological conditions. Consequently hidden information characteristic to each class of molecule, particularly of the ERK pathway, and of the process dynamics were extracted. The presented method of analysis is a suitable tool to identify discrete variations in mechanotransduction dynamics attributed to the pathophysiology of osteoporosis. Additionally, the analyses can be used in the future to complement *in vitro* experiments tailored to explore spatiotemporal effects of treatments on mechanotransduction, and if they mimic bio-mechanical stimuli.

Supplementary information

Supplementary information accompanies this paper at <https://doi.org/10.1186/s12859-020-3394-0>.

Additional file 1: Figure S1. Cytoplasmic and nuclear biochemical reactions.

Abbreviations

ABM: Agent-based model; ACS: Activation Cycle Switch; BR: Bone remodelling; ECM: Extracellular matrix; EGF: Epidermal growth factor; ERK: Extracellular signal-regulated kinase; iPTH: PTH analogue; Mech-ABM: Hybrid mechanical-ABM model; MEK: MAPK/Erk kinase; OB: Osteoblast; OC: osteoclast; OCy: Osteocyte; pERK: Phosphorylated ERK; PTHR: PTH receptor; Raf: Rapidly Accelerated Fibrosarcoma; SIP: Signal interim period; WTD: Waiting Time Distribution

Acknowledgements

We would like to thank Miss Yasmin Beladaci for her effort in generating preliminary data that assisted in parameter evaluation.

Authors' contributions

GA and AS wrote the manuscript, GA designed and performed the model analysis, and executed the simulations; AS, TMS and DL designed the Mech-ABM; AS lead the *in silico* experimentation design and sensitivity analysis parameter selection, EDA and AS contributed equally towards *in silico* experimentation refinement; the design of the model's analysis framework, and data interpretation. DL, TMS, EDA and AS edited the manuscript. All authors have read and approved the manuscript.

Funding

This study was funded by the Engineering and Physical Sciences Research Council (EPSRC), Frontier Engineering Multiscale modelling of the skeleton: EP/K03877X/1. The funders did not participate in the design of the study and collection, analysis, and interpretation of data and in writing the manuscript.

Availability of data and materials

We will release our code, data and appropriate materials under the Creative Commons Attribution License. These are available on Google Drive at this link: https://drive.google.com/drive/folders/1Q0HFvumv6NTxpBXfKQerR93l-4_t9LAu?usp=sharing

Ethics approval and consent to participate

Not applicable.

Consent for publication

Not applicable.

Competing interests

The authors declare that they have no competing interests.

Author details

¹Department of Oncology and Metabolism, University of Sheffield, Sheffield, UK. ²Insigneo Institute of In Silico Medicine, University of Sheffield, Sheffield, UK. ³Department of Mechanical Engineering, University of Sheffield, Sheffield, UK.

Received: 9 August 2019 Accepted: 4 February 2020

Published online: 18 March 2020

References

- Burge R, Worley D, Johansen A, Bose U. The cost of osteoporotic fractures in the United Kingdom. *Value in Health*. 2001;4(2):66–7.
- Yap AS, Duszyc K, Viasnoff V. Mechanosensing and Mechanotransduction at Cell–Cell Junctions. *Cold Spring Harb Perspect Biol*. 2018;10(8). <https://doi.org/10.1101/cshperspect.a028761>.
- Friedl P, Mayor R. Tuning Collective Cell Migration by Cell–Cell Junction Regulation. *Cold Spring Harb Perspect Biol*. 2017;9(4). <https://doi.org/10.1101/cshperspect.a029199>.
- Capulli M, Paone R, Rucci N. Osteoblast and osteocyte: games without frontiers. *Arch Biochem Biophys*. 2014;561:3–12.
- Alonso JL, Goldmann WH. Cellular mechanotransduction. *Transport*. 2016;1:7.
- Harris AR, Jreij P, Fletcher DA. Mechanotransduction by the actin cytoskeleton: converting mechanical stimuli into biochemical signals. *Annu Rev Biophys*. 2016;47(1):617–31.
- Martino F, Perestrelo AR, Vinarský V, Pagliari S, Forte G. Cellular Mechanotransduction: From Tension to Function. *Front Physiol*. 2018;9(824). <https://doi.org/10.3389/fphys.2018.00824>.
- Humphrey JD, Dufresne ER, Schwartz MA. Mechanotransduction and extracellular matrix homeostasis. *Nat Rev Mol Cell Biol*. 2014;15:802.
- Papachroni KK, Karatzas DN, Papavassiliou KA, Basdra EK, Papavassiliou AG. Mechanotransduction in osteoblast regulation and bone disease. *Trends Mol Med*. 2009;15(5):208–16.
- Vincent TL. Targeting mechanotransduction pathways in osteoarthritis: a focus on the pericellular matrix. *Curr Opin Pharmacol*. 2013;13(3):449–54.
- Batra N, Burra S, Siller-Jackson AJ, Gu S, Xia X, Weber GF, DeSimone D, Bonewald LF, Lafer EM, Sprague E, et al. Mechanical stress-activated integrin $\alpha 5 \beta 1$ induces opening of connexin 43 hemichannels. *Proc Natl Acad Sci*. 2012;109(9):3359–64.
- Buo AM, Stains JP. Gap junctional regulation of signal transduction in bone cells. *FEBS Lett*. 2014;588(8):1315–21.
- Jiang JX, Siller-Jackson AJ, Burra S. Roles of gap junctions and hemichannels in bone cell functions and in signal transmission of mechanical stress. *Frontiers Biosci*. 2007;12:1450–62.
- Okamoto T, Suzuki K. The role of gap junction-mediated endothelial cell–cell interaction in the crosstalk between inflammation and blood coagulation. *Int J Mol Sci*. 2017;18(11):2254.
- Charras G, Yap AS. Tensile forces and Mechanotransduction at cell–cell junctions. *Curr Biol*. 2018;28(8):R445–57.
- Oh S-H, Kim J-W, Kim Y, Lee MN, Kook M-S, Choi EY, Im S-Y, Koh J-T. The extracellular matrix protein Edil3 stimulates osteoblast differentiation through the integrin $\alpha 5 \beta 1$ /ERK/Runx2 pathway. *PLoS One*. 2017;12(11):e0188749.
- Yavropoulou MP, Yovos JG. The molecular basis of bone mechanotransduction. *J Musculoskelet Neuronal Interact*. 2016;16(3):221–36.
- Muhamed I, Chowdhury F, Maruthamuthu V. Biophysical Tools to Study Cellular Mechanotransduction. *Bioengineering (Basel, Switzerland)*. 2017;4(1):12.
- Wang N. Review of cellular mechanotransduction. *J Phys D Appl Phys*. 2017;50(23):233002.
- D'Antonio G, Macklin P, Preziosi L. An agent-based model for elasto-plastic mechanical interactions between cells, basement membrane and extracellular matrix. *Mathematical Biosci Eng*. 2013;10(1):75–101.

21. Shams H, Soheilipour M, Peyro M, Moussavi-Baygi R, Mofrad MRK. Looking "under the Hood" of cellular Mechanotransduction with computational tools: a systems biomechanics approach across multiple scales. *ACS Biomaterials Science & Engineering*. 2017;3(11):2712–26.
22. Barreto S, Clausen CH, Perrault CM, Fletcher DA, Lacroix D. A multi-structural single cell model of force-induced interactions of cytoskeletal components. *Biomaterials*. 2013;34(26):6119–26.
23. Livne A, Bouchbinder E, Geiger B. Cell reorientation under cyclic stretching. *Nat Commun*. 2014;5:3938.
24. Luo T, Mohan K, Iglesias PA, Robinson DN. Molecular mechanisms of cellular mechanosensing. *Nat Mater*. 2013;12:1064.
25. Jurchenko C, Salaita KS. Lighting up the force: investigating mechanisms of Mechanotransduction using fluorescent tension probes. *Mol Cell Biol*. 2015; 35(15):2570–82.
26. Lin X, Shi Y, Cao Y, Liu W. Recent progress in stem cell differentiation directed by material and mechanical cues. *Biomed Mater*. 2016;11(1):014109.
27. Bartocci E, Lió P. Computational modeling, formal analysis, and tools for systems biology. *PLoS Comput Biol*. 2016;12(1):e1004591.
28. Fisher J, Henzinger TA. Executable cell biology. *Nat Biotechnol*. 2007;25: 1239.
29. Peng T, Liu L, MacLean AL, Wong CW, Zhao W, Nie Q. A mathematical model of mechanotransduction reveals how mechanical memory regulates mesenchymal stem cell fate decisions. *BMC Syst Biol*. 2017;11(1):55.
30. Klann M, Koepl H. Spatial simulations in systems biology: from molecules to cells. *Int J Mol Sci*. 2012;13(6):7798–827.
31. Klann MT, Lapin A, Reuss M. Agent-based simulation of reactions in the crowded and structured intracellular environment: influence of mobility and location of the reactants. *BMC Syst Biol*. 2011;5(1):71.
32. Shuaib A, Motan D, Bhattacharya P, McNabb A, Skerry TM, Lacroix D. Heterogeneity in the mechanical properties of integrins determines mechanotransduction dynamics in bone osteoblasts. *Sci Rep*. 2019; 9(1): 13113–13113.
33. Glen CM, Kemp ML, Voit EO. Agent-based modeling of morphogenetic systems: advantages and challenges. *PLoS Comput Biol*. 2019;15(3): e1006577.
34. Holland JH, Miller JH. Artificial adaptive agents in economic theory. *Am Econ Rev*. 1991;81(2):365–70.
35. Pogson M, Holcombe M, Smallwood R, Qvarnstrom E. Introducing spatial information into predictive NF- κ B Modelling – an agent-based approach. *PLoS One*. 2008;3(6):e2367.
36. Pogson M, Smallwood R, Qvarnstrom E, Holcombe M. Formal agent-based modelling of intracellular chemical interactions. *Biosystems*. 2006;85(1):37–45.
37. Legewie S, Schoeberl B, Blüthgen N, Herzog H. Competing docking interactions can bring about bistability in the MAPK cascade. *Biophys J*. 2007;93(7):2279–88.
38. Purutcuoglu V, Wit E. Estimating network kinetics of the MAPK/ERK pathway using biochemical data. *Math Probl Eng*. 2012:1–34.
39. Shuaib A, Hartwell A, Kiss-Toth E, Holcombe M. Multi-compartmentalisation in the MAPK Signalling pathway contributes to the emergence of oscillatory behaviour and to ultrasensitivity. *PLoS One*. 2016;11(5):e0156139.
40. Fujioka A, Terai K, Itoh RE, Aoki K, Nakamura T, Kuroda S, Nishida E, Matsuda M. Dynamics of the Ras/ERK MAPK Cascade as monitored by fluorescent probes. *J Biol Chem*. 2006;281(13):8917–26.
41. Radhakrishnan K, Edwards JS, Lidke DS, Jovin TM, Wilson BS, Oliver JM. Sensitivity analysis predicts that the ERK-pMEK interaction regulates ERK nuclear translocation. *IET Syst Biol*. 2009;3(5):329–41.
42. Sokolov IM, Klafter J. From diffusion to anomalous diffusion: a century after Einstein's Brownian motion. *Chaos: An Interdisciplinary Journal of Nonlinear Science*. 2005;15(2):026103.
43. Gorenflo R, Mainardi F. Subordination pathways to fractional diffusion. *Eur Physical J Special Topics*. 2011;193(1):119–32.
44. Ascolani G, Bologna M, Grigolini P. Subordination to periodic processes and synchronization. *Physica A: Statistical Mechanics and its Applications*. 2009; 388(13):2727–40.
45. Bohara G, West BJ, Grigolini P. Bridging waves and crucial events in the dynamics of the brain. *Front Physiol*. 2018;9:1174.
46. Montroll EW, Weiss GH. Random walks on lattices. II. *J Mathematical Physics*. 1965;6(2):167–81.
47. Dickman R. Reweighting in nonequilibrium simulations. *Phys Rev E*. 1999; 60(3):R2441–4.
48. Mullen CA, Haugh MG, Schaffler MB, Majeska RJ, McNamara LM. Osteocyte differentiation is regulated by extracellular matrix stiffness and intercellular separation. *J Mech Behav Biomed Mater*. 2013;28:183–94.
49. Schneider GB, Zaharias R, Stanford C. Osteoblast integrin adhesion and signaling regulate mineralization. *J Dent Res*. 2001;80(6):1540–4.
50. Shekaran A, Shoemaker JT, Kavanaugh TE, Lin AS, LaPlaca MC, Fan Y, Guldberg RE, Garcia AJ. The effect of conditional inactivation of beta 1 integrins using twist 2 Cre, Osterix Cre and osteocalcin Cre lines on skeletal phenotype. *Bone*. 2014;68:131–41.
51. Fullstone G, Wood J, Holcombe M, Battaglia G. Modelling the transport of nanoparticles under blood flow using an agent-based approach. *Sci Rep*. 2015;5:10649.
52. Richmond P, Walker D, Coakley S, Romano D. High performance cellular level agent-based simulation with FLAME for the GPU. *Brief Bioinform*. 2010;11(3):334–47.
53. Rhodes DM, Holcombe M, Qvarnstrom EE. Reducing complexity in an agent based reaction model—benefits and limitations of simplifications in relation to run time and system level output. *Biosystems*. 2016;147:21–7.
54. Liu L, Zong C, Li B, Shen D, Tang Z, Chen J, Zheng Q, Tong X, Gao C, Wang J. The interaction between β 1 integrins and ERK1/2 in osteogenic differentiation of human mesenchymal stem cells under fluid shear stress modelled by a perfusion system. *J Tissue Eng Regen Med*. 2014;8(2):85–96.
55. Yang JM, Bhattacharya S, West-Foyle H, Hung CF, Wu TC, Iglesias PA, Huang CH. Integrating chemical and mechanical signals through dynamic coupling between cellular protrusions and pulsed ERK activation. *Nat Commun*. 2018;9(1):4673.
56. Grabowski F, Czyż P, Kocharczyk M, Lipniacki T. Limits to the rate of information transmission through the MAPK pathway. *J R Soc Interface*. 2019;16(152):20180792.
57. Skerry T. Neurotransmitters in bone. Introduction. *J Musculoskelet Neuronal Interact*. 2002;2(5):401–3.
58. Skerry TM. The role of glutamate in the regulation of bone mass and architecture. *J Musculoskelet Neuronal Interact*. 2008;8(2):166–73.
59. Skerry TM, Taylor AF. Glutamate signalling in bone. *Curr Pharm Des*. 2001;7(8):737–50.
60. Judex S, Lei X, Han D, Rubin C. Low-magnitude mechanical signals that stimulate bone formation in the ovariectomized rat are dependent on the applied frequency but not on the strain magnitude. *J Biomech*. 2007;40(6): 1333–9.
61. Mogil RJ, Kaste SC, Ferry RJ Jr, Hudson MM, Mulrooney DA, Howell CR, Partin RE, Srivastava DK, Robison LL, Ness KK. Effect of low-magnitude, high-frequency mechanical stimulation on BMD among young childhood Cancer survivors: a randomized clinical trial. *JAMA oncology*. 2016;2(7):908–14.
62. Rubin C, Turner AS, Bain S, Mallinckrodt C, McLeod K. Anabolism: low mechanical signals strengthen long bones. *Nature*. 2001;412(6847):603.
63. Hwang J-H, Lee D-H, Byun MR, Kim AR, Kim KM, Park JI, Oh HT, Hwang ES, Lee KB, Hong J-H. Nanotopological plate stimulates osteogenic differentiation through TAZ activation. *Sci Rep*. 2017;7(1):3632.
64. Yan YX, Gong YW, Guo Y, Lv Q, Guo C, Zhuang Y, Zhang Y, Li R, Zhang XZ. Mechanical strain regulates osteoblast proliferation through integrin-mediated ERK activation. *PLoS One*. 2012;7(4):e35709.
65. Mitra T, Menon SN, Sinha S. Emergent memory in cell signaling: persistent adaptive dynamics in cascades can arise from the diversity of relaxation time-scales. *Sci Rep*. 2018;8(1):13230.
66. Gesty-Palmer D, Flannery P, Yuan L, Corsino L, Spurney R, Lefkowitz RJ, Luttrell LM. A β -Arrestin-Biased Agonist of the Parathyroid Hormone Receptor (PTH1R) Promotes Bone Formation Independent of G Protein Activation. *Sci Transl Med*. 2009;1(1):1ra1.
67. Gesty-Palmer D, Luttrell LM: 'biasing' the parathyroid hormone receptor: a novel anabolic approach to increasing bone mass? *Br J Pharmacol*. 2011; 164(1):59–67.
68. Frith JE, Kusuma GD, Carthew J, Li F, Cloonan N, Gomez GA, Cooper-White JJ. Mechanically-sensitive miRNAs bias human mesenchymal stem cell fate via mTOR signalling. *Nat Commun*. 2018;9(1):257.
69. Hwang J-H, Byun MR, Kim AR, Kim KM, Cho HJ, Lee YH, Kim J, Jeong MG, Hwang ES, Hong J-H. Extracellular matrix stiffness regulates Osteogenic differentiation through MAPK activation. *PLoS One*. 2015;10(8):e0135519.
70. Li CX, Talele NP, Boo S, Koehler A, Knee-Walden E, Balestrini JL, Speight P, Kapus A, Hinz B. MicroRNA-21 preserves the fibrotic mechanical memory of mesenchymal stem cells. *Nat Mater*. 2016;16:379.

71. Yang C, Tibbitt MW, Basta L, Anseth KS. Mechanical memory and dosing influence stem cell fate. *Nat Mater*. 2014;13:645.
72. Li S, Li F, Zou S, Zhang L, Bai Y. PTH1R signalling regulates the mechanotransduction process of cementoblasts under cyclic tensile stress. *Eur J Orthod*. 2018;40(5):537–43.
73. Ali AM, Atmaj J, Van Oosterwijk N, Groves MR, Domling A. Stapled peptides inhibitors: a new window for target drug discovery. *Comput Struct Biotechnol J*. 2019;17:263–81.
74. Arkin MR, Tang Y, Wells JA. Small-molecule inhibitors of protein-protein interactions: progressing toward the reality. *Chem Biol*. 2014;21(9):1102–14.
75. Zarzycka B, Kuenemann MA, Miteva MA, Nicolaes GAF, Vriend G, Sperandio O. Stabilization of protein–protein interaction complexes through small molecules. *Drug Discov Today*. 2016;21(1):48–57.
76. Kochanczyk M, Kocieniewski P, Kozłowska E, Jaruszewicz-Blonska J, Sparta B, Pargett M, Albeck JG, Hlavacek WS, Lipniacki T. Relaxation oscillations and hierarchy of feedbacks in MAPK signaling. *Sci Rep*. 2017;7:38244.
77. Magdevska L, Mraz M, Zimic N, Moškon M. Initial state perturbations as a validation method for data-driven fuzzy models of cellular networks. *BMC Bioinformatics*. 2018;19(1):333.

Publisher's Note

Springer Nature remains neutral with regard to jurisdictional claims in published maps and institutional affiliations.

Ready to submit your research? Choose BMC and benefit from:

- fast, convenient online submission
- thorough peer review by experienced researchers in your field
- rapid publication on acceptance
- support for research data, including large and complex data types
- gold Open Access which fosters wider collaboration and increased citations
- maximum visibility for your research: over 100M website views per year

At BMC, research is always in progress.

Learn more biomedcentral.com/submissions

